Bayesian rupture imaging in a complex medium: The 29 May 2012 Emilia, Northern Italy, earthquake

Mathieu Causse, Giovanna Cultrera, Ludovic Moreau, André Herrero, Erika Schiappapietra, Françoise Courboulex

AGU PUBLICATIONS

Geophysical Research Letters

RESEARCH LETTER
10.1002/2017GL074698

Key Points:
- An interpolation scheme of aftershock waveforms is developed to model near-field wave propagation for a fault embedded in a complex medium
- Bayesian inversion of the strong motion data recorded during the 2012 Emilia earthquake reveals a notably slow rupture and slip velocity
- Despite the wave propagation complexity, the near-field data are particularly well reproduced using 15 rupture parameters

Supporting Information:
- Supporting Information S1

Correspondence to:
M. Causse,
mathieu.causse@univ-grenoble-alpes.fr

Citation:
Causse, M., G. Cultrera, L. Moreau, A. Herrero, E. Schiappapietra, and F. Courboulex (2017), Bayesian rupture imaging in a complex medium: The 29 May 2012 Emilia, Northern Italy, earthquake, *Geophys. Res. Lett.*, *44*, 7783–7792, doi:10.1002/2017GL074698.

Received 23 JUN 2017
Accepted 26 JUL 2017
Accepted article online 31 JUL 2017
Published online 12 AUG 2017

Bayesian rupture imaging in a complex medium: The 29 May 2012 Emilia, Northern Italy, earthquake

Mathieu Causse[1], Giovanna Cultrera[2], Ludovic Moreau[1], André Herrero[2], Erika Schiappapietra[1], and Françoise Courboulex[3]

[1]Université Grenoble Alpes, Université Savoie Mont Blanc, CNRS, IRD, IFSTTAR, ISTerre, Grenoble, France, [2]Istituto Nazionale di Geofisica e Vulcanologia, Rome, Italy, [3]Université Côte d'Azur, CNRS, IRD, Observatoire de la Côte d'Azur, Géoazur, Valbonne, France

Abstract We develop a new approach to image earthquake rupture from strong motion data. We use a large data set of aftershock waveforms, interpolated over the seismic fault to obtain Green's function approximations. Next we deploy a Bayesian inversion method to characterize the slip distribution, the rupture velocity, the slip duration, and their uncertainties induced by errors in the Green's functions. The method is applied to the 29 May 2012 M_w 6 Emilia earthquake, which ruptured a fault buried below the Po Plain sediments (Northern Italy). Despite the particularly complex wave propagation, the near-field strong motion observations are well reproduced with 15 rupture parameters. The rupture and slip velocities were notably slow (~0.5 V_s and <0.5 m/s, respectively), implying that the fault was difficult to break. This method opens some perspectives for earthquake rupture studies in areas where numerical simulations suffer from imprecise knowledge of the velocity structure.

1. Introduction

In May 2012 the largest seismic crisis ever recorded in the Po Plain (Northern Italy) by modern digital seismometers occurred. It started on 20 May with a M_w 6.1 event, followed by a second M_w 6.0 main shock on 29 May [*Cheloni et al.*, 2016] and hundreds of other aftershocks. This seismic sequence took place on a south dipping blind thrust fault system (Ferrara arc) in the Emilia-Romagna region, covered by the quaternary sediment of the Po Plain. During the 2012 Emilia main shocks, Peak Ground Accelerations larger than 0.5 g were recorded. Damage was widespread, causing 27 fatalities and a high economic loss due to the concentration of industrial activities.

Moderate to large earthquakes are infrequent in this area, which is characterized by a low-to-moderate level of seismicity as compared to Central and Southern Italy. It has remained almost silent since the M 5.5 1570 Ferrara earthquake, with the exception of sporadic small- to medium-magnitude earthquakes [*Graziani et al.*, 2015]. This long return period results from a slow strain rate (north-south shortening of ~1 mm/yr) [*Maesano et al.*, 2015].

The goal of this study is to analyze the rupture properties of those infrequent events, by using an exceptional data set of near-fault strong motion recordings. We focus on the second M_w 6.0 main shock of 29 May, which has been recorded by strong motion stations from the Italian Strong Motion Network (Rete Accelerometrica Nazionale, RAN) and by temporary stations installed by the Istituto Nazionale di Geofisica e Vulcanologia after the first main shock, providing a unique data set of 11 high-quality near-field records at epicentral distances lower than 30 km [*Bordoni et al.*, 2012; *de Nardis et al.*, 2014].

The strong motion analysis shows that near-source records are particularly complex, characterized by a mix of body waves and strong surface waves [*Luzi et al.*, 2013; *Cultrera et al.*, 2014; *Dujardin et al.*, 2016]. This arises because the quaternary deposits of the Po Plain covering the seismic fault of the M_w 6.0 shock are spatially variable, with a thickness ranging from about 200 m to 2 km [*Paolucci et al.*, 2015; *Molinari et al.*, 2015]. In addition, site effects studies report amplification peaks down to very low frequencies (peaks at 0.15 and 0.7 Hz) [*Milana et al.*, 2014]. The wave propagation complexity explains why finite source analyses of the 2012 Emilia earthquakes have been essentially based on static ground displacement measurements (GPS and/or interferometric synthetic aperture radar (InSAR) data) [e.g., *Cheloni et al.*, 2016; *Pezzo et al.*, 2013; *Tizzani et al.*, 2013] or broadband ground motion data at regional distances [*Cesca et al.*, 2013]. Such analyses do not provide high-resolution space-time evolution of the

rupture propagation on the fault and hence relevant clues on the observed ground shaking. Using the strong motion data and 3-D numerical Green's functions, *Paolucci et al.* [2015] determined by trial and error the slip distribution and the rupture velocity of the second M_w 6.0 main shock. Nevertheless, this study highlights the difficulty to match the observed strong motion records despite the use of 3-D numerical Green's functions.

We develop a new approach for the inversion of strong motion data in complex media like the Po Plain. The data set consists of more than 130 earthquakes recorded at 11 three-component strong motion stations (Table S1 in the supporting information). We do not compute the Green's functions numerically. Instead, we employ small aftershock waveforms (referred to as AWs in the following) as empirical Green's functions [e.g., *Miyake et al.*, 2003; *Hutchings et al.*, 2007; *Del Gaudio et al.*, 2015]. Using a large database of aftershocks, we propose a simple strategy to interpolate the AWs over the fault plane and build a forward model. We next deploy a Bayesian inversion technique to retrieve the model parameters describing the rupture propagation on the fault (final slip distribution, rupture velocity, and local slip duration). These parameters are represented by their posterior distributions, that is, suites of models fitting the data within a certain uncertainty range, providing information about the resolution of the inferred rupture features.

2. Forward Problem: Green's Functions Approximation and Rupture Parameterization

2.1. Aftershock Selection and Processing

For each strong motion station, we select a suite of aftershocks with local magnitude M_L between 2.7 and 4. This magnitude choice ensures a satisfactory signal-to-noise ratio at low frequency ($<$0.2 Hz) while limiting the possibility of complex source effects. These aftershocks were relocated using a 3D velocity model [*Chiarabba et al.*, 2014]. We discard all the aftershocks located at a distance larger than 2 km from the assumed seismic fault (details about the seismic fault position can be found in section 3). We also discard AWs containing multiple aftershock signals within a time window of 20 to 40 s, depending on the station. Each AW is then processed according to the following procedure: (1) band-pass filtering in the frequency range 0.2–1 Hz, ensuring a signal-to-noise ratio larger than 3, and (2) deconvolution by a Brune's (1970) source model. For that purpose, we compute the corner frequency by matching a "ω-square" source spectrum to the observed displacement spectra and compute the seismic moment assuming that the local and the moment magnitude are equal. Since a Brune source spectrum has a zero phase shift, the deconvolution only affects the amplitude spectra and does not generate noncausal effects in the time series [*Hutchings et al.*, 2007]. We thus obtain an approximation of the local Green's function.

2.2. Interpolation of Aftershock Waveforms

The stability of the forward model computation requires that the Green's functions are determined over the seismic fault on a fine grid (400 m grid spacing is chosen), while the spatial distribution of aftershocks is heterogeneous. In order to interpolate the AWs onto an evenly spaced grid, we propose the following procedure (Figure 1a). For each fault point (i, j), we select all AWs located at a distance smaller than 3 km. If no AW is available, the closest one is considered. The amplitudes are scaled by $d_{\mathrm{epi}}/d_{i,j}$, where d_{epi} is the epicentral distance and $d_{i,j}$ is the distance between the fault point and the considered station, to account for the S wave geometrical spreading. In case multiple AWs are selected, they are aligned using cross correlation, choosing the closest AW as a reference. All the AWs having a coefficient of correlation with the reference AW lower than 0.7 are discarded. The remaining AWs are stacked and averaged. An evident advantage of stacking several AWs is to average potential uncertainties induced by inappropriate source deconvolution, uncertainty in the aftershock location, and variability of the aftershock focal mechanisms. Finally, the resulting average AW is shifted so as to get the correct S wave arrival time. The procedure used to compute the S wave arrival time over the seismic fault is described and illustrated for station MIR01 in Text S1 and Figure S1 in the supporting information, while Figure S2 shows an example of selected waveforms and resulting Green's function approximation between a fault point (i, j) and station MIR01. Moreover, Texts S1 and S2 explain how the uncertainties associated with each Green's function, which will be incorporated in the Bayesian rupture inversion, are accounted for. Finally, the number of

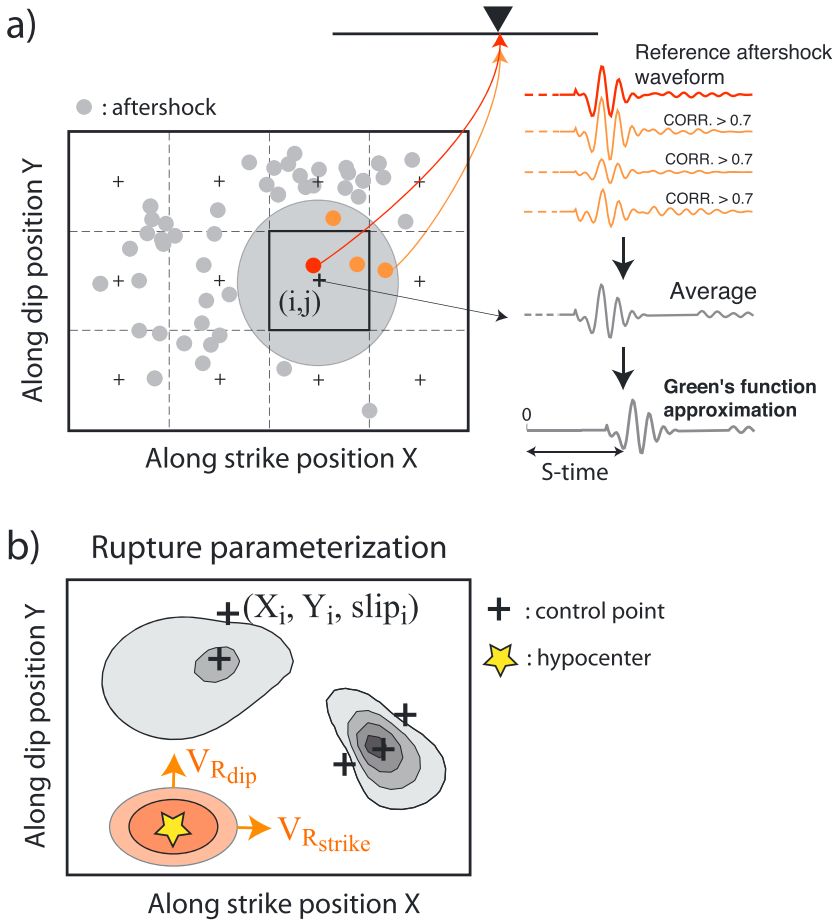

Figure 1. Diagrams illustrating the forward model computation. (a) Green's function computation. The orange and red circles indicate the aftershocks selected within the volume represented by the gray circle and used for computing the Green's function between the fault point (*i*, *j*) and the target station. (b) Parameterization of the rupture space-time evolution. The gray surfaces depict the final slip distribution obtained by interpolation between the slip values at the control points, whose positions are inversion parameters. In this example, five control points are used.

AWs used for each station to compute the Green's functions or the *S* wave arrival time is reported in Table S1.

2.3. Rupture Parameterization

The parameters characterizing the spatiotemporal evolution of the rupture propagation on the seismic fault are described in Figure 1b. We assume that the rupture propagates from the hypocenter at a constant rupture velocity. Nevertheless, we distinguish between the along-strike and along-dip rupture velocities (VR_{strike} and VR_{dip}, respectively). The temporal evolution of the local slip is represented by a regularized Yoffe function [*Tinti et al.*, 2005], with a constant slip duration (rise time) over the fault plane. In order to account for the spatial heterogeneity of the final slip distribution, we use the concept of "control points" (Figure 1b) [e.g., *Moreau et al.*, 2014]: the final slip values are not defined on a regular grid; instead, we define the slip values at some control points, which can move over the fault plane. The final slip values are then interpolated on the fine grid used for the Green's function computation, using biharmonic spline interpolation and setting the fault edge slip values to zero. This formalism is beneficial because the control point density varies spatially and naturally adapts to the local complexity of the parameters and to the resolving power of the data [e.g., *Dettmer et al.*, 2014; *Michelini*, 1995]. Thus, complex features of the slip distribution can be captured with few parameters.

Finally, for a given set of source parameters, the ground velocity can be computed at each station by convolving the local slip rate functions and the Green's function and summing up the contributions of each grid point.

2.4. Seismic Fault

Geological and geophysical subsurface information suggests that the seismic fault that broke during the 29 May shock has a listric geometry, with a strike angle of ~95° and dip angles varying from ~35° at the hypocenter to ~65° at the top of the fault at ~3 km [*Maesano et al.*, 2015]. Such a geometry is also evidenced by numerical modeling of ground deformation InSAR measurements [*Tizzani et al.*, 2013], and it is confirmed by the near-fault strong motion data. First, the observation of the vertical velocities shows a change of the *P* wave polarity between the stations MIR08 and MIR04. By means of point source simulations in the 1-D medium proposed by *Paolucci et al.* [2015], we obtained by trial and error that this change of polarity is reproduced if the dip angle at the hypocentral depth ranges from 39° to 45°. Second, the proper modeling of the fault-perpendicular velocity pulses observed at stations MIR02 and MRN implies a steeper shallow fault dip angle of the order of 60° [*Paolucci et al.,* 2015]. We then build a simplified model of the seismic fault proposed by *Maesano et al.* [2015], composed of two planes with a strike angle of 95° and with a dip angle of 40° between 12 and 8.5 km depth and 60° between 8.5 and 3 km. The deepest plane contains the 3-D relocated hypocenter of *Chiarabba et al.* [2014].

3. Bayesian Inversion of Rupture Parameters

3.1. Accounting for Modeling Uncertainty Using the Bayes' Theorem

In order to account for the uncertainty in the Green's functions, we perform a Bayesian estimation of the rupture parameters [e.g., *Minson et al.*, 2013; *Duputel et al.*, 2014; *Razafindrakoto and Mai*, 2014; *Hallo and Gallovič*, 2016]. Bayes' theorem offers a framework for providing not a single solution but suites of solutions fitting the data with an acceptable level of fit, given the data uncertainty. These suites of solutions are represented by the posterior distribution of the model parameters, given by

$$\rho(\boldsymbol{m}|\boldsymbol{d}) = \frac{f(\boldsymbol{d}|\boldsymbol{m})\rho(\boldsymbol{m})}{\rho(\boldsymbol{d})}, \tag{1}$$

where $\boldsymbol{d}$ and $\boldsymbol{m}$ represent the model and the data space, respectively, $f(\boldsymbol{d}|\boldsymbol{m})$ is the likelihood function, $\rho(\boldsymbol{m})$ is the prior distribution, and $\rho(\boldsymbol{d})$ is the marginal likelihood function. As such, the posterior distribution expresses the conditional probability of the model parameter values based on evidence from the data and from prior assumptions.

We assume the following prior information for the rupture parameters: (1) the average hypocenter position matches the one proposed by *Chiarabba et al.* [2014], but it is allowed to vary by ±1.5 km in the along-strike and along-dip directions; (2) the values of VR_{strike} and VR_{dip} are uniformly distributed in the range [1 km/s–5 km/s]; (3) the rise time values have a uniform distribution in the range [0.3 s–3 s]; and (4) the local final slip values are uniformly distributed between 0 and D_{max} = 1.1 m, where D_{max} is the maximum expected final slip value for a M_w 6 earthquake [*McGarr and Fletcher*, 2003].

The data uncertainty is expressed in the likelihood function, assumed to be Gaussian [*Tarantola*, 2005]:

$$f(\boldsymbol{m}|\boldsymbol{d}) = c\exp[-S(\boldsymbol{m})] \tag{2}$$

$$S(\boldsymbol{m}) = \frac{1}{2}\left\{[G(\boldsymbol{m}) - \boldsymbol{d}]^T C_D^{-1}[G(\boldsymbol{m}) - \boldsymbol{d}]\right\}, \tag{3}$$

where $S(m)$ is the cost function quantifying the level of fit between the computed ground velocity and the data and C_D is the data covariance matrix representing the uncertainty in the data. Formally, C_D contains errors introduced by the data (for instance, noise in the observations) and by imperfect modeling [e.g., *Duputel et al.*, 2012]. In this study the data noise is marginal in the analyzed frequency range (0.2–1 Hz) and we consider only uncertainty in the Green's functions.

3.2. Inverse Problem Solving

The model space is explored by performing a Markov chain using the Metropolis algorithm [*Metropolis et al.*, 1953]. This iterative approach is a random walk, in which the "bad" models are unlikely to be accepted. A model $\boldsymbol{m}_i$ at iteration i is considered bad if the ratio of the likelihood functions $f(\boldsymbol{d}|\boldsymbol{m}_i)/f(\boldsymbol{d}|\boldsymbol{m}_{i-1})$ return a probability lower than α, where α is a random number sampled between 0 and 1 from a uniform distribution. This random walk converges toward the posterior distribution. In order to speed up the convergence, it is essential that the initial model is close to the global optimum. We then follow a two-step approach. First, we seek

for the global optimum (that is, the maximum likelihood model), deploying simulated annealing global optimization [*Kirkpatrick et al*., 1983]. The obtained model is referred to as $\boldsymbol{m}_{\mathbf{best}}$. We ran the algorithm considering various numbers of control points of the slip distribution and obtained that using more than four control points does not improve the data fit. This number is thus set to 4, leading to 15 parameters to describe the rupture process. The convergence of the simulated annealing algorithm is shown in Figure S3. Second, we use the Metropolis algorithm to explore the model space around the model $\boldsymbol{m}_{\mathbf{best}}$ and generate samples of the posterior distribution. To this end, the observed data $\boldsymbol{d}$ in equation (3) is replaced by $G(\boldsymbol{m}_{best})$. The covariance matrix C_D can then be rigorously determined as follows: we compute 500 realizations of forward models, considering the rupture parameters $\boldsymbol{m}_{\mathbf{best}}$ and by randomly perturbating the *S* arrival times and peak velocities of the Green's functions according to their distributions (Texts S1 and S2). The resulting population of synthetic velocities is used to compute C_D. We checked that the distribution of the residuals $G(\boldsymbol{m})$-$G(\boldsymbol{m}_{best})$ is Gaussian, as required by equations (2) and (3). It is noteworthy that we assume uncorrelated data, which implies that C_D is diagonal. Finally, the random walk consists of 100,000 iterations with an acceptance rate of 50% (in agreement with the rate of 30%–50% suggested by *Tarantola* [2005]). To minimize the effect of autocorrelation between samples induced by the random walk, we select only every 100th sample. We are then left with 1000 uncorrelated samples.

3.3. Results

The above mentioned technique is deployed to obtain a rupture model for the 29 May 2012 Emilia earthquake from the strong motion data. Because the AWs time correction pertains only to the *S* waves, we do not consider the vertical component of ground motion, characterized by energetic *P* waves [*Milana et al.*, 2014]. Moreover, in order to eliminate some of the late surface waves with phase velocities smaller than V_s, we consider only the first 10 to 15 s of the horizontal components, depending on the station. Finally, each time history is normalized by its maximum absolute value to avoid underweighting of the farthest stations and the EW components, which have a lower amplitude.

Our favored slip distribution (Figure 2a) shows that the rupture had a seismic moment of 1.3e18 N m, equivalent to a M_w 6.0 event. This is consistent with the regional centroid moment tensor solution (http://rcmt2.bo.ingv.it/), GPS, and InSAR data analyses [*Cheloni et al*., 2016; *Tizzani et al*., 2013] and inversion of teleseismic body waves (SCARDEC method) [*Vallée et al*., 2011]. The slip distribution consists of two patches, the shallowest also revealed by GPS and InSAR data [*Cheloni et al*., 2016]. Maximum slip of ~0.9 m occurs at ~6 km depth. The observation of the marginal posterior distributions of local slip reveals that this patch is well resolved, while the deepest patch is poorly resolved, as indicated by the low values of the ratio between the mean slip and the 95% confidence interval (~0.3). The inversion systematically places one of the four control points at the bottom of the shallowest patch, with a small slip value, indicating that a weak amount of slip beneath the patch is required to fit the data. This feature is common to all the models. Interestingly, the bottom edge of the patch coincides with a concentration of $M_L > 3$ aftershocks (Figure 2a).

The analysis of the rupture velocity and rise time values is, however, more enlightening (Figure 2b). The maximum likelihood values of VR_{strike} and VR_{dip} are 0.45 V_s and 0.5 V_s, respectively, which is significantly lower than the commonly observed rupture velocities, between 0.65 V_s and 0.85 V_s [*Heaton*, 1990]. The analysis of the joint distributions reveals a correlation between VR_{strike} and the rise time (CORR. = 0.61) and VR_{dip} and the rise time (CORR. = 0.32). Despite this bias, the marginal posterior distributions indicates with a probability of ~95% that VR_{strike} and VR_{dip} are lower than 0.65 V_s, confirming that the rupture propagated slowly. In addition, the rise time values, whose maximum likelihood is about 1.7 s, are far above the reported values for a $M < 6.5$ event, which are essentially lower than 1 s [*Somerville et al*., 1999]. This means that the fault slipped slowly, with a velocity lower than 0.5 m/s over a large part of the fault. It is noteworthy that the obtained rupture velocity and rise time values are ~20% lower and a factor of ~3 larger than the ones reported by *Paolucci et al*. [2015], respectively.

Despite the simplicity of the rupture hypotheses (constant rupture velocity and rise time) and the wave propagation complexity, the proposed model matches the data fairly well (Figure 3). The level of fit is remarkable at stations MIR02, MRN, and SAN0, located above the seismic fault. The NS components of the velocity at MIR02 and MRN, dominated by a strong pulse induced by updip directivity, are the best reproduced (coefficient of correlation >0.9). The correlation is also good at MIR01, situated just above the hypocenter, even

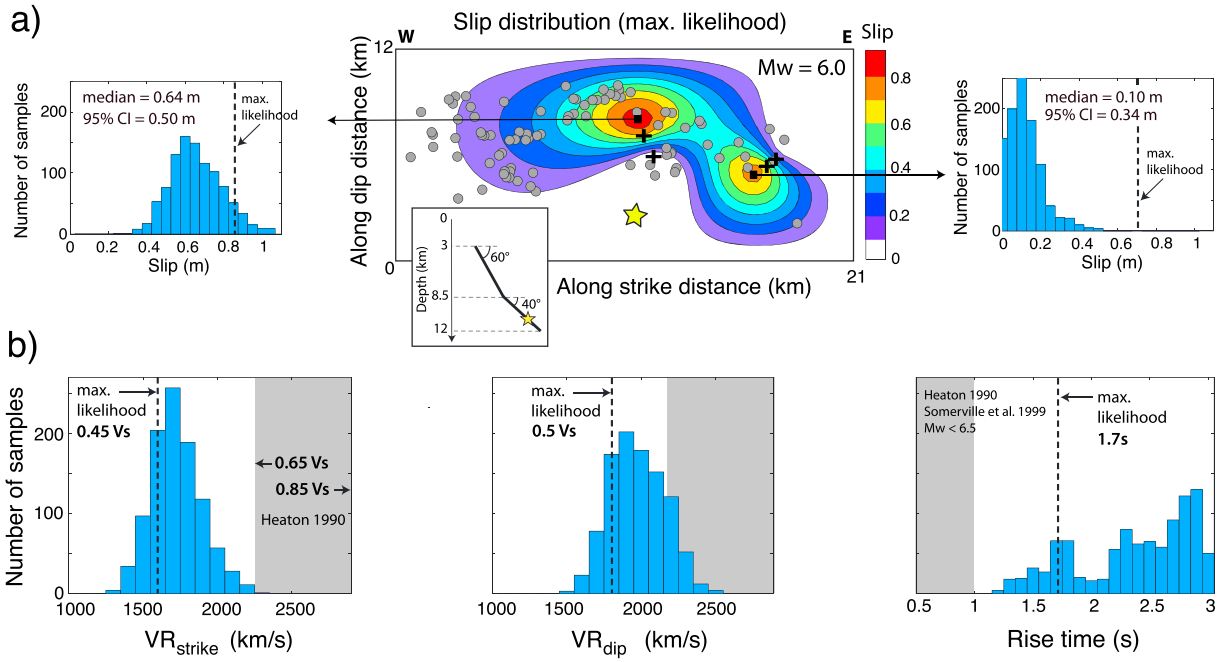

Figure 2. Inferred rupture model of the 29 May 2012 Emilia earthquake. (a) Final slip distribution (maximum likelihood) obtained using four control points, represented by black crosses. The view angle is perpendicular to the upper rupture plane. The gray circles depict the aftershocks with $M_l > 3$ recorded during 3 weeks and located less than 2 km away from the assumed seismic fault. The histograms represent the posterior distributions of slip at the points indicated by the arrows. The median slip values and the 95% confidence interval are shown. (b) Posterior distributions of the along-strike rupture velocity, along-dip rupture velocity, and rise time. The gray areas indicate the rupture velocity range reported by *Heaton* [1990] and the range of rise time values reported by *Somerville et al.* [1999] for $M_w < 6.5$ events.

though the amplitude is significantly underestimated. This discrepancy may be explained by a strong spatial variability of the *S* wave radiation pattern along the dip above the hypocenter area associated with a too sparse AW sampling, or by additional complexity of the rupture propagation, like spatial variability of the rupture velocity. Stations located farther away from the fault generally have a lower level of fit and a larger uncertainty, due to the increasing ground motion complexity and the decreasing number of available AWs (Table S1 in the supporting information). Some surface wave trains are nevertheless particularly well reproduced, as, for instance, at stations MOG0, NVL, and RAV0 (NS components), even though they are not included in the inverted time windows (Figure 3).

3.4. Simple Dynamic Interpretation

During the fault rupture, part of the available elastic energy is supplied to the crack tip for the rupture to propagate. The energy used by the rupture is called fracture energy. Basic theory on earthquake rupture dynamics [e.g., *Freund*, 1990], as well as heterogeneous 3-D dynamic rupture simulations [e.g., *Schmedes et al.*, 2010], shows that both rupture velocity and slip velocity decrease as the ratio between the fracture energy and the available elastic energy increases. The low average rupture and slip velocities observed during the 29 May 2012 Emilia earthquake imply that the fault was hard to break and that the fault strength was high in comparison to the initial stress level.

4. Discussion

The complexity of strong motion observations can arise from complex path effects or/and complex rupture propagation. Inappropriate Green's function inevitably leads to biased rupture images and can reveal complex rupture features that are only artifacts [e.g., *Gallovič et al.*, 2015; *Mai et al.*, 2016]. Our inversion results show that simple assumptions about the rupture process (represented by 15 parameters), coupled with aftershock-based Green's functions, which naturally contain information about propagation and site effects between the source and the receiver, are adequate to explain the near-source observation complexity. This

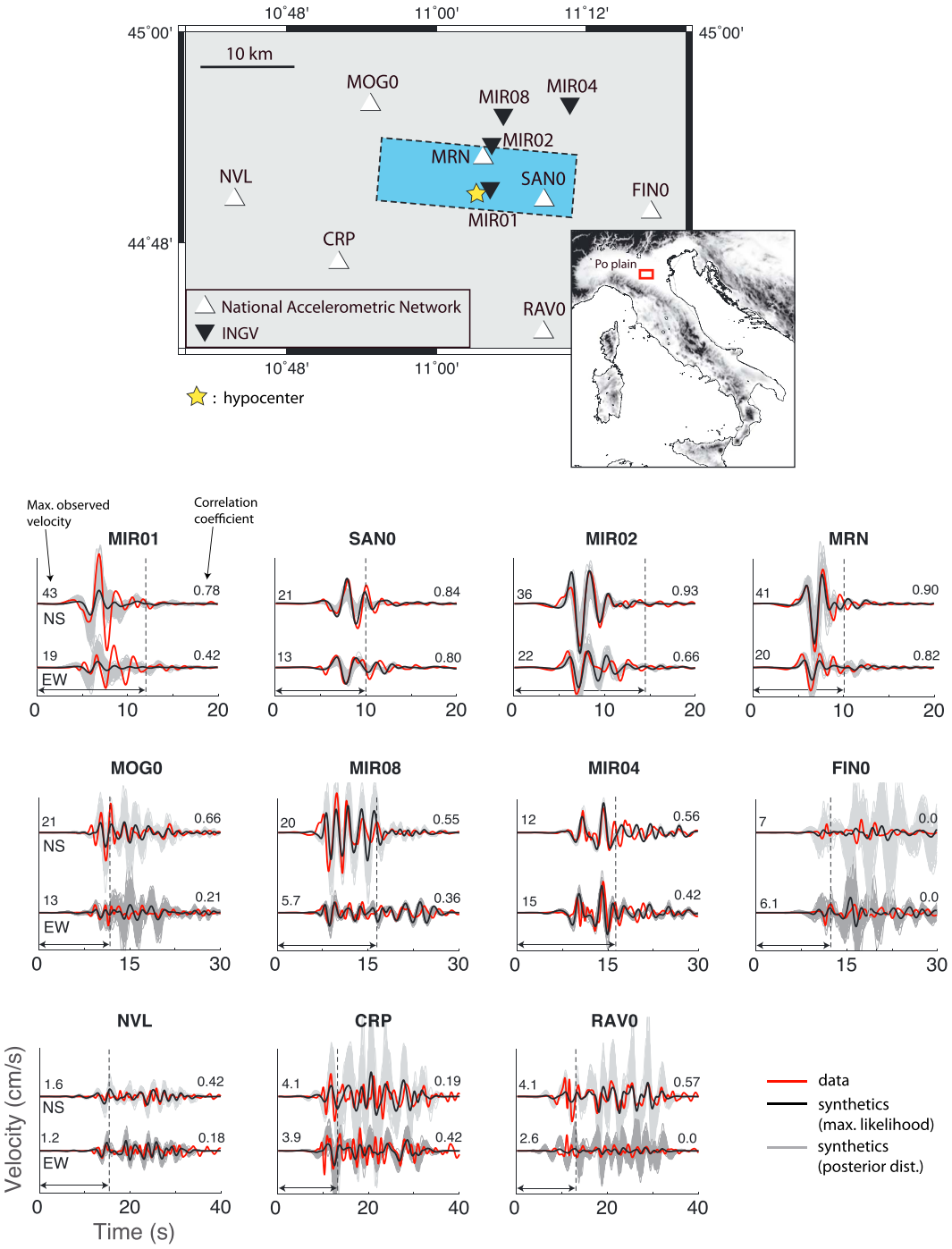

Figure 3. Top: map of the 11 strong motion stations used for the rupture inversion. The blue rectangle represents the approximate surface rupture projection. Bottom: comparison between observed velocities and synthetics (0.2–1 Hz). The horizontal arrows indicate the time window considered in the inversion.

seems to indicate that nonlinear propagation effects, which are not accounted for, did not play a significant role in the considered frequency band (0.2–1 Hz) and at the considered stations. Besides, we have carried out complementary inversion tests showing that the use of simplistic 1-D Green's functions is obviously not suitable to fit the observations. Figure S4 illustrates the considerable discrepancy between observed velocities and 1-D point source simulations using the velocity model of *Milana et al.* [2014] for a M_w 3.7 aftershock. Furthermore, introducing a higher level of complexity in the rupture parameterization may

reveal additional properties (for instance, spatial variations of the rupture velocity) but would also reduce the inversion resolution. Regarding the slip complexity, the use of additional control points does not enhance the data fit (see section 3.2).

It is generally observed that a slow rupture and a slow slip tend to generate weak near-field ground motions. Surprisingly, the near-field ground velocities recorded during the earthquake are, however, in agreement with Italian empirical ground motion predictions for sediment sites [*Luzi et al.*, 2013]. One reason may be the particularly large site effects reported at low frequency [*Milana et al.*, 2014], which is accounted for by using the AWs. Another explanation may lie in the rupture process itself. The corner frequency of the earthquake (obtained from Brune's spectrum matching the moment rate function spectrum) is 0.2 Hz, which is exactly the average value reported in the global analysis of *Allmann and Shearer* [2009] for a M_w 6 event. The corner frequency f_c provides a measure of the high-frequency source energy and is such that $f_c \propto VR \cdot \Delta\tau^{1/3}$, where $\Delta\tau$ is the average static stress drop [e.g., *Courboulex et al.*, 2016]. Hence, the slow rupture velocity was probably counterbalanced by a large stress drop, which contributed to amplify the ground motion [e.g., *Cotton et al.*, 2013]. Slow rupture propagation (0.5 V_s) coupled with a large stress drop was also observed during the 1999 M_w 7.1 Hector Mine earthquake [*Kaverina et al.*, 2002]. Furthermore, anticorrelation between rupture velocity and stress drop has been recently proposed as a possible source property to explain the observed between-event ground motion variability [*Causse and Song*, 2015]. Note that we prefer this simple f_c-based interpretation to an analysis of the absolute stress drop value, the latter being affected by large uncertainties: first, the relationship between f_c and stress drop strongly varies with the source model assumptions [e.g., *Kaneko and Shearer*, 2015] and second, slip distribution-based measurements depend on the resolution of the slip images [*Adams et al.*, 2017] and open the issue of how to average stress drop over the fault, leading to an additional source of uncertainty [*Noda et al.*, 2013].

An important question raised by this study is the link between the properties of the fault and the rupture process. In the Emilia area, the long recurrence period of earthquakes induced by the slow convergence rate may favor the fault sealing. Kinetic modeling of fracture porosity around active fault indicates timescales of fracture sealing of 10^3–10^4 years between 2 and 10 km for carbonate rock [*Renard et al.*, 2000]. Long interseismic periods may then promote the strengthening of barriers, which may increase fracture energy and slowdown the rupture, at least locally, and map into the slow average rupture velocity. The analysis of ruptures on similar fault systems will be necessary to confirm this mechanism. Some other mechanisms like the failure of multiple fault segments have been reported to explain slow average rupture velocities [*Zhang et al.*, 2017]. For the Emilia case, the complexity of the fault geometry suggested by geophysical and geological observations [*Maesano et al.*, 2015] may have also contributed to slowdown the rupture.

5. Conclusion

We developed a new approach for inverting earthquake rupture parameters in complex media from strong motion data. This approach makes use of aftershock waveforms, interpolated over the fault plane, to compute Green's function approximations and build the forward model. These aftershocks naturally contain information about propagation and site effect between the source and the receivers, under the assumption of soil response linearity. The rupture parameters (along-strike and along-dip rupture velocities, rise time, and slip distribution) are then determined by means of a Bayesian inversion, leading to suites of rupture parameters mapping the uncertainty in the Green's function.

The method was applied to the 29 May 2012 M_w 6.0 Emilia earthquake, using an exceptional data set of 11 near-field strong motion stations. Despite the particularly complex wave propagation of the Po Plain, the observations can be fairly well fit using 15 rupture parameters (four slip control points, constant rupture velocity, and rise time). This seems to indicate that nonlinear site effects played only a minor role in the considered frequency range of 0.2–1 Hz and at the considered stations. The rupture propagated slowly (speed of ~0.5 V_s), and the fault slipped slowly (speed lower than 0.5 m/s). This implies that most of the available strain energy was used as fracture energy to supply the rupture propagation. Although the rupture was slow, the corner frequency is similar to the average value given by worldwide analyses [*Allmann and Shearer*, 2009], indicating a high stress drop. This method provides opportunities for earthquake rupture studies in areas where numerical simulations suffer from imprecise knowledge of the velocity structure.

Acknowledgments

We thank Chiara d'Ambrogi for providing information about the seismic fault geometry and Pasquale De Gori for providing the 3-D aftershock localizations. We also thank Luis Fabian Bonilla, Michel Bouchon, Antonella Cirella, and Frantisek Gallovic for fruitful discussions, and Gavin Hayes and an anonymous reviewer for their careful reviews. This study has been supported by AGIR-POLE-PAGE (Université Grenoble Alpes) and Tellus-ALEAS (CNRS-INSU) research funds. The strong motion waveforms used in this paper are available at the RAN website (http://ran.protezionecivile.it) and in the EIDA archive (http://eida.rm.ingv.it).

References

Adams, M., C. Twardzik, and C. Ji (2017), Exploring the uncertainty range of coseismic stress drop estimations of large earthquakes using finite fault inversions, *Geophys. J. Int.*, *208*, 86–100, doi:10.1093/gji/ggw374.

Allmann, B. P., and P. M. Shearer (2009), Global variations of stress drop for moderate to large earthquakes, *J. Geophys. Res.*, *114*, B01310, doi:10.1029/2008JB005821.

Bordoni, P., et al. (2012), Preliminary results from EMERSITO, the rapid response network for site effect studies, *Ann. Geophys.*, *55*(4), 599–607, doi:10.4401/ag-6153.

Causse, M., and S. G. Song (2015), Are stress drop and rupture velocity of earthquakes independent? Insight from observed ground motion variability, *Geophys. Res. Lett.*, *42*, 7383–7389, doi:10.1002/2015GL064793.

Cesca, S., T. Braun, F. Maccaferri, L. Passarelli, E. Rivalta, and T. Dahm (2013), Source modelling of the *M*5–6 Emilia-Romagna, Italy, earthquakes (2012 May 20–29), *Geophys. J. Int.*, *193*, 1658–1672, doi:10.1093/gji/ggt069.

Cheloni, D., R. Giuliani, N. D'Agostino, M. Mattone, M. Bonano, G. Fornaro, R. Lanari, D. Reale, and S. Atzori (2016), New insights into fault activation and stress transfer between en echelon thrusts: The 2012 Emilia, Northern Italy, earthquake sequence, *J. Geophys. Res. Solid Earth*, *121*, 4742–4766, doi:10.1002/2016JB012823.

Chiarabba, C., P. De Gori, L. Improta, F. P. Lucente, M. Moretti, A. Govoni, M. Di Bona, L. Margheriti, A. Marchetti, and A. Nardi (2014), Frontal compression along the Apennines thrust system: The Emilia 2012 example from seismicity to crustal structure, *J. Geodyn.*, *82*, 98–109, doi:10.1016/j.jog.2014.09.003.

Cotton, F., R. Archuleta, and M. Causse (2013), What is sigma of the stress drop?, *Seismol. Res. Lett.*, *84*(1), 42–48.

Courboulex, F., M. Vallée, M. Causse, and A. Chounet (2016), Stress-drop variability of shallow earthquakes extracted from a global database of source time functions, *Seismol. Res. Lett.*, *87*, 912–918, doi:10.1785/0220150283.

Cultrera, G., L. Faenza, C. Meletti, V. D'Amico, A. Michelini, and A. Amato (2014), Shakemaps uncertainties and their effects in the post-seismic actions for the 2012 Emilia (Italy) earthquakes, *Bull. Earthquake Eng.*, *12*(5), 2147–2164, doi:10.1007/s10518-013-9577-6.

Del Gaudio, S., M. Causse, and G. Festa (2015), Broad-band strong motion simulations coupling k-square kinematic source models with empirical Green's functions: The 2009 L'Aquila earthquake, *Geophys. J. Int.*, *203*(1), 720–736.

de Nardis, R., L. Filippi, G. Costa, P. Suhadolc, M. Nicoletti, and G. Lavecchia (2014), Strong motion recorded during the Emilia 2012 thrust earthquakes (Northern Italy): A comprehensive analysis, *Bull. Earthquake Eng.*, *12*, 2117–2145, doi:10.1007/s10518-014-9614-0.

Dettmer, J., R. Benavente, P. R. Cummins, and M. Sambridge (2014), Trans-dimensional finite-fault inversion, *Geophys. J. Int.*, *199*, 735–751, doi:10.1093/gji/ggu280.

Dujardin, A., M. Causse, F. Courboulex, and P. Traversa (2016), Simulation of the basin effects in the Po plain during the Emilia-Romagna seismic sequence (2012) using empirical Green's functions, *Pure Appl. Geophys.*, *173*, 1993–2010, doi:10.1007/s00024-015-1233-4.

Duputel, Z., P. S. Agram, M. Simons, S. E. Minson, and J. L. Beck (2014), Accounting for prediction uncertainty when inferring subsurface fault slip, *Geophys. J. Int.*, *197*, 464–482, doi:10.1093/gji/ggt517.

Duputel, Z., L. Rivera, Y. Fukahata, and H. Kanamori (2012), Uncertainty estimations for seismic source inversions: Uncertainty estimations for source inversions, *Geophys. J. Int.*, *190*, 1243–1256, doi:10.1111/j.1365-246X.2012.05554.x.

Freund, L. B. (1990), *Dynamic Fracture Mechanics*, Cambridge Univ. Press, New York.

Gallovič, F., W. Imperatori, and P. M. Mai (2015), Effects of three-dimensional crustal structure and smoothing constraint on earthquake slip inversions: Case study of the M_w 6.3 2009 L'Aquila earthquake, *J. Geophys. Res. Solid Earth*, *120*, 428–449, doi:10.1002/2014JB011650.

Graziani, L., F. Bernardini, C. Castellano, S. Del Mese, E. Ercolani, A. Rossi, A. Tertulliani, and M. Vecchi (2015), The 2012 Emilia (Northern Italy) earthquake sequence: An attempt of historical reading, *J. Seismol.*, *19*, 371–387, doi:10.1007/s10950-014-9471-y.

Hallo, M., and F. Gallovič (2016), Fast and cheap approximation of Green functions uncertainty for waveform-based earthquake source inversions, *Geophys. J. Int.*, *207*, 1012–1029, doi:10.1093/gji/ggw320.

Heaton, T. H. (1990), Evidence for and implications of self-healing pulses of slip in earthquake rupture, *Phys. Earth Planet. Inter.*, *64*, 1–20.

Hutchings, L., E. Ioannidou, W. Foxall, N. Voulgaris, J. Savy, I. Kalogeras, L. Scognamiglio, and G. Stavrakakis (2007), A physically based strong ground-motion prediction methodology: Application to PSHA and the 1999 M_w = 6.0 Athens earthquake, *Geophys. J. Int.*, *168*(2), 659–680.

Kaneko, Y., and P. M. Shearer (2015), Variability of seismic source spectra, estimated stress drop, and radiated energy, derived from cohesive-zone models of symmetrical and asymmetrical circular and elliptical ruptures, *J. Geophys. Res. Solid Earth*, *120*, 1053–1079, doi:10.1002/2014JB011642.

Kaverina, A., D. Dreger, and E. Price (2002), The combined inversion of seismic and geodetic data for the source process of the 16 October 1999 M_w 7.1 Hector Mine, California, earthquake, *Bull. Seismol. Soc. Am.*, *92*, 1266–1280.

Kirkpatrick, S., C. D. Gelatt, and M. P. Vecchi (1983), Optimization by simulated annealing, *Science*, *220*(4598), 671–680.

Luzi, L., et al. (2013), Overview on the strong-motion data recorded during the May–June 2012 Emilia seismic sequence, *Seismol. Res. Lett.*, *84*, 629–644, doi:10.1785/0220120154.

Maesano, F. E., C. D'Ambrogi, P. Burrato, and G. Toscani (2015), Slip-rates of blind thrusts in slow deforming areas: Examples from the Po Plain (Italy), *Tectonophysics*, *643*, 8–25, doi:10.1016/j.tecto.2014.12.007.

Mai, P. M., et al. (2016), The earthquake-source inversion validation (SIV) project, *Seismol. Res. Lett.*, *87*, 690–708, doi:10.1785/0220150231.

McGarr, A., and J. B. Fletcher (2003), Maximum slip in earthquake fault zones, apparent stress, and stick-slip friction, *Bull. Seismol. Soc. Am.*, *93*, 2355–2362.

Metropolis, N., A. W. Rosenbluth, M. N. Rosenbluth, A. H. Teller, and E. Teller (1953), Equation of state calculations by fast computing machines, *J. Chem. Phys.*, *21*, 1087–1092, doi:10.1063/1.1699114.

Michelini, A. (1995), An adaptive-grid formalism for traveltime tomography, *Geophys. J. Int.*, *121*, 489–510.

Milana, G., P. Bordoni, F. Cara, G. Di Giulio, S. Hailemikael, and A. Rovelli (2014), 1D velocity structure of the Po River plain (Northern Italy) assessed by combining strong motion and ambient noise data, *Bull. Earthquake Eng.*, *12*, 2195–2209, doi:10.1007/s10518-013-9483-y.

Minson, S. E., M. Simons, and J. L. Beck (2013), Bayesian inversion for finite fault earthquake source models. I—Theory and algorithm, *Geophys. J. Int.*, *194*(3), 1701–1726.

Miyake, H., T. Iwata, and K. Irikura (2003), Source characterization for broadband ground-motion simulation: Kinematic heterogeneous source model and strong motion generation area, *Bull. Seismol. Soc. Am.*, *93*, 2531–2545.

Molinari, I., A. Argnani, A. Morelli, and P. Basini (2015), Development and testing of a 3D seismic velocity model of the Po Plain sedimentary basin, Italy, *Bull. Seismol. Soc. Am.*, *105*, 753–764, doi:10.1785/0120140204.

Moreau, L., A. J. Hunter, A. Velichko, and P. D. Wilcox (2014), 3-D reconstruction of sub-wavelength scatterers from the measurement of scattered fields in elastic waveguides, *IEEE Trans. Ultrason. Ferroelectr. Freq. Control*, *61*(11), 1864–1879.

Noda, H., N. Lapusta, and H. Kanamori (2013), Comparison of average stress drop measures for ruptures with heterogeneous stress change and implications for earthquake physics, *Geophys. J. Int.*, *193*, 1691–1712, doi:10.1093/gji/ggt074.

Paolucci, R., I. Mazzieri, and C. Smerzini (2015), Anatomy of strong ground motion: Near-source records and three-dimensional physics-based numerical simulations of the M_w 6.0 2012 May 29 Po Plain earthquake, Italy, *Geophys. J. Int.*, *203*, 2001–2020, doi:10.1093/gji/ggv405.

Pezzo, G., et al. (2013), Coseismic deformation and source modeling of the May 2012 Emilia (Northern Italy) earthquakes, *Seismol. Res. Lett.*, *84*, 645–655.

Razafindrakoto, H. N. T., and P. M. Mai (2014), Uncertainty in earthquake source imaging due to variations in source time function and Earth structure, *Bull. Seismol. Soc. Am.*, *104*, 855–874, doi:10.1785/0120130195.

Renard, F., J.-P. Gratier, and B. Jamtveit (2000), Kinetics of crack-sealing, intergranular pressure solution, and compaction around active faults, *J. Struct. Geol.*, *22*, 1395–1407.

Schmedes, J., R. J. Archuleta, and D. Lavallée (2010), Correlation of earthquake source parameters inferred from dynamic rupture simulations, *J. Geophys. Res.*, *115*, B03304, doi:10.1029/2009JB006689.

Somerville, P., et al. (1999), Characterizing crustal earthquake slip models for the prediction of strong ground motion, *Seismol. Res. Lett.*, *70*(1), 59–80.

Tarantola, A. (2005), *Inverse Problem Theory and Methods for Model Parameter Estimation*, Society for Industrial and Applied Mathematics, Philadelphia, Pennsylvania.

Tinti, E., E. Fukuyama, P. Alessio, and C. Massimo (2005), A kinematic source-time function compatible with earthquake dynamics, *Bull. Seismol. Soc. Am.*, *95*, 1211–1223, doi:10.1785/0120040177.

Tizzani, P., et al. (2013), New insights into the 2012 Emilia (Italy) seismic sequence through advanced numerical modeling of ground deformation InSAR measurements: Modeling of the 2012 Emilia seismic sequence, *Geophys. Res. Lett.*, *40*, 1971–1977, doi:10.1002/grl.50290.

Vallée, M., J. Charléty, A. M. G. Ferreira, B. Delouis, and J. Vergoz (2011), SCARDEC: A new technique for the rapid determination of seismic moment magnitude, focal mechanism and source time functions for large earthquakes using body-wave deconvolution: Wave deconvolution and earthquake parameters, *Geophys. J. Int.*, *184*, 338–358, doi:10.1111/j.1365-246X.2010.04836.x.

Zhang, H., K. D. Koper, K. Pankow, and Z. Ge (2017), Imaging the 2016 M_w 7.8 Kaikoura, New Zealand earthquake with teleseismic *P* waves: A cascading rupture across multiple faults, *Geophys. Res. Lett.*, *44*, 4790–4798, doi:10.1002/2017GL073461.